1766 *Biochemistry* **2010,** *49,* 1766–1775
DOI: 10.1021/bi901902e

BIOCHEMISTRY
including biophysical chemistry & molecular biology
Article

Pyrene Fluorescence Analysis Offers New Insights into the Conformation of the Lipoprotein-Binding Domain of Human Apolipoprotein E[†]

Arti B. Patel, Panupon Khumsupan, and Vasanthy Narayanaswami*

Department of Chemistry and Biochemistry, 1250 Bellflower Boulevard, California State University Long Beach, Long Beach, California 90840

Received November 5, 2009; Revised Manuscript Received January 4, 2010

ABSTRACT: The C-terminal domain (CT) of apolipoprotein E (apoE), a critical protein involved in cholesterol transport in the plasma and brain, plays an important role in high-affinity lipoprotein binding. Although high-resolution structural information is available for the N-terminal domain of apoE, the structural organization of the CT (residues 201−299) is largely unknown. In this study, we employ site-specific fluorescence labeling with pyrene maleimide to gain insight into the structure and conformation of apoE CT in its naturally self-associated state in buffer at physiologically relevant concentrations (5−50 μg/mL). Pyrene is a highly sensitive fluorophore that reports on spatial proximity between desired sites by displaying unique spectral features. Pyrene was covalently attached to single cysteine-containing recombinant human apoE CT at position 223 or 255 to probe the first predicted helical segment and at position 277 to monitor the terminal predicted helical segment. Regardless of the location of the probe, all three pyrene-labeled apoE CT variants display an intense and dramatic fluorescence excimer band at 460 nm, a signature feature of pyrene, which indicates that two pyrene moieties are within 10 Å of each other. In addition, an intense peak at 387 nm (indicative of a highly hydrophobic environment) was noted in all cases. Fluorescence emission quenching by potassium iodide indicates that the accessibility to the probes was restricted at these locations. The possibility that the hydrophobicity of the pyrene moiety was the driving force for helix−helix interaction was excluded because pyrene located at position 209, which is predicted to be located in a nonhelical segment, did not display the above intense unique features. Lastly, denaturation studies suggest that the terminal helix unfolds prior to the first predicted helix in apoE CT. Our studies indicate that there are extensive intermolecular helix−helix contacts throughout the entire CT in the lipid-free state with two apoE CT molecules oriented parallel to each other to form a dimer, which dimerizes further to yield a tetramer. Such an organization allows helix−helix interactions to be replaced by helix−lipid interactions upon encountering a lipoprotein surface, with the terminal helix likely initiating the binding interaction. This study presents the possibility of employing pyrene fluorophores as powerful new alternatives to obtain conformational information of proteins at physiologically relevant concentrations.

Apolipoprotein E (apoE)[1] is an antiatherogenic protein that plays a critical role in regulating plasma and brain cholesterol homeostasis (*1*−*5*). It is an exchangeable protein component of triglyceride-rich lipoproteins and a subclass of high-density lipoprotein (HDL) in plasma. In addition, apoE is one of the major apolipoproteins in the central nervous system, where it has been localized on HDL-sized particles (*6*, *7*). ApoE also functions in reverse cholesterol transport in atherosclerosis, a process involving transport of cholesterol from the peripheral tissues to the liver for eventual disposal via the bile (*8*−*10*). In humans, three major isoforms of apoE have been noted, with variations in the amino acids at positions 112 and 158: apoE2 has Cys while apoE4 has Arg at these locations; apoE3 has a Cys and an Arg at these positions, respectively. Importantly, the apoE4 isoform in humans is considered a significant risk factor for developing Alzheimer's disease (*5*, *11*).

ApoE is composed of 299 residues that are organized as two independently folded domains: a 22 kDa N-terminal domain (residues 1−191) that mediates high-affinity binding to the low-density lipoprotein receptor family of proteins and a 10 kDa C-terminal domain (CT) that bears high-affinity binding sites for lipids and lipoprotein surfaces (*12*−*15*). The high-resolution structure of the N-terminal domain of all three major isoforms was identified more than 15 years ago (*16*−*18*). The crystallization of a segment of the CT domain encompassing residues 223−272 was reported (*19*); however, we do not have an understanding of the high-resolution structure of this isolated domain or that of the intact protein yet. Structural predictions indicate that residues 210−266 form a long class A amphipathic α-helix, while residues 268−289 form a class G* helix (*20*, *21*) (Figure 1A). Class A

[†]This work was funded by a grant in aid from the American Heart Association (07551374), SCAC Award and funding for research from CSULB, the Drake Family Trust and Tobacco Related Disease Research Program (TRDRP 17RT-0165) (V.N.), TRDRP CHDAS (17RT-0165H) (A.B.P.), and an award from Women & Philanthropy (P.K.).

*Address correspondence to this author. Tel: (562) 985-4953. Fax: (562) 985-8557. E-mail: vnaraya2@csulb.edu.

[1]Abbreviations: apoE, apolipoprotein E; CD, circular dichroism; CT, C-terminal domain; DTT, dithiothreitol; GdnHCl, guanidine hydrochloride; GS-pyrene, pyrene-labeled glutathione; HDL, high-density lipoprotein; IAEDANS, 5-((((2-iodoacetyl)amino)ethyl)amino)naphthalene-1-sulfonic acid; KI, potassium iodide; K_{SV}, Stern−Volmer quenching constant; NPM, *N*-(1-pyrene)maleimide; PBS, phosphate-buffered saline, 10 mM sodium phosphate, pH 7.4, and 150 mM NaCl; TCEP, tris(2-carboxyethyl)phosphine; TFE, trifluoroethanol; WT, wild type.

 Published on Web 01/14/2010

amphipathic helices are characterized by clustering of positively charged amino acid residues at the polar−nonpolar interface and negatively charged residues at the center of the polar face (*20*, *22*). On the other hand, class G* helices lack clustering of charged residues but have a random distribution of negative and positive residues around the perimeter of the polar face. Segments bearing class G* helices are believed to be involved in protein−protein interaction and subunit formation (*21*, *22*). Consistent with this prediction, substitution of a few bulky residues, F257, W264, V269, L279, and V287, toward the C-terminal end of the apoE CT with small polar residues resulted in a protein that could not be cross-linked, suggesting that these residues are important for apoE self-association (*23*, *24*). Further, based on sedimentation equilibrium studies on C-terminal truncated apoE, it was proposed that the segment encompassing the class G* helix is likely involved in apoE3 self-association to form a tetramer in the absence of lipids (*25*, *26*) (Figure 1A). It was also indicated that residues 225−272 are involved in directing the preference of lipoprotein binding; however, the spatial disposition of this helix with respect to the neighboring apoE molecule in the absence of lipids is not known. Previously, our laboratory proposed that the segment encompassing residues 210−266 likely forms an intermolecular coiled-coil helix (*27*). This was based on secondary structure analysis by circular dichroism (CD) spectroscopy. In the present study, we exploited the spatially sensitive spectral features of the fluorophore pyrene to obtain insights into the tertiary and quaternary conformation of residues 201−299. We report that the entire CT of apoE makes extensive intermolecular helix−helix contact to form a parallel dimer, which dimerizes further to form a tetramer at physiologically relevant concentrations.

MATERIALS AND METHODS

Materials. *N*-(1-Pyrene)maleimide (NPM), pyrene, 5-((((2-iodoacetyl)amino)ethyl)amino)naphthalene-1-sulfonic acid, 1,5-IAEDANS (IAEDANS), and tris(2-carboxyethyl)phosphine (TCEP) were obtained from Invitrogen (Eugene, OR). Dithiothreitol (DTT), guanidine hydrochloride (GdnHCl), potassium iodide (KI), sodium thiosulfate, and glutathione were obtained from Fisher Scientific (Fair Lawn, NJ). Trifluoroethanol (TFE) was purchased from Sigma Aldrich (St. Louis, MO). All solvents used were of analytical grade.

Expression, Isolation, and Purification of apoE CT. Wild-type (WT) apoE CT comprising residues 201−299 and apoE CT variants A209C, S223C, E255C, and A277C with single substituted cysteine residues at the indicated locations were obtained as described previously (*28*). Recombinant apoE CT bearing a hexa-His tag at the N-terminal end to facilitate purification was overexpressed in a bacterial expression system, isolated, and purified using a Ni-affinity matrix (Hi-Trap chelating column; GE Healthcare) as described earlier (*27*, *28*). Protein purity was verified by SDS−PAGE analysis using a 4−20% acrylamide gradient.

Circular Dichroism (CD) Spectroscopy. CD measurements were performed on a Jasco 810 spectropolarimeter. Far-UV CD scans were recorded between 185 and 260 nm in 10 mM ammonium bicarbonate buffer, pH 7.4, using protein concentrations of 0.2 mg/mL as determined by absorbance at 280 nm (molar extinction coefficient of apoE CT at 280 nm = 16500 M^{-1} cm^{-1}). Far-UV profiles were the average of three independent scans, with a response time of 1 s and bandwidth of 1 nm. The path length of the cuvette was 0.1 cm. The molar ellipticity ([θ]) in deg cm^2 $dmol^{-1}$ at 222 nm was obtained using the equation:

$$[\theta]_{222\text{nm}} = \text{MRW}(\theta)/10lc$$

where MRW is the mean residue weight of apoE CT (obtained by dividing molecular weight by the number of residues) calculated to be 115.03, θ is the measured ellipticity in degrees at 222 nm, l is the cuvette path length (in cm), and c is the protein concentration (in g/mL). The percent α-helix content was calculated as described by others (*29*):

$$\%\ \alpha\text{-helix} = (-[\theta_{222\text{nm}}] + 3000)/39000$$

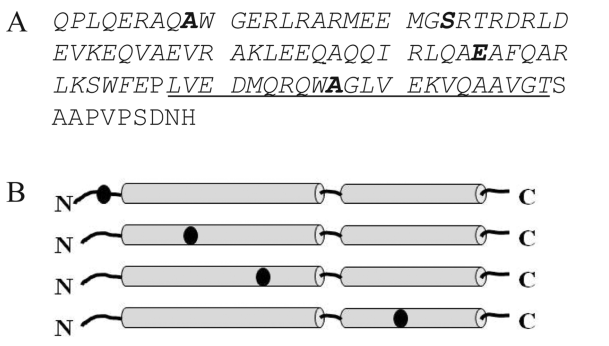

FIGURE 1: Design and site-directed labeling of apoE CT constructs. (A) Sequence of apoE CT (residues 201−299). Underlined segment (residues 268−289) indicates proposed self-association sites based on C-terminal truncation studies (*25*). Italicized segments 210−266 and 268−289 represent class A and G* helices, respectively. Bold letters specify positions 209, 223, 255, and 277, which were substituted by Cys for site-directed labeling. (B) The predicted amphipathic α-helical segments are schematically shown as cylinders, and the tentative location of the probes is shown as black ovals.

Disulfide Bond Formation. The purified proteins were unfolded in the presence of 3 M GdnHCl and a 2-fold molar excess of a reducing agent, dithiothreitol (DTT). Excess GdnHCl and DTT were removed by dialysis against 10 mM sodium phosphate, pH 7.4, containing 150 mM NaCl (phosphate-buffered saline, PBS) for 48 h at 4 °C with three changes in buffer. The refolded samples were examined by SDS−PAGE analysis under nonreducing and reducing conditions.

Fluorescence Labeling. ApoE CT A209C, S223C, E255C, or A277C was initially preincubated with a 5-fold molar excess of TCEP in the presence of 3 M GdnHCl for 4 h at 37 °C in 10 mM ammonium bicarbonate, pH 7.4, to reduce existing intermolecular disulfide bonds. This was followed by incubation with a 10-fold molar excess of NPM for 16 h at 37 °C or IAEDANS for 16 h at 37 °C and removal of excess unbound TCEP, GdnHCl, and fluorophore by passing the mixture through a Ni-affinity Hi-Trap chelating column. In addition, glutathione, a control tripeptide bearing a single Cys (γ-Glu-Cys-Gly or GSH), was labeled with NPM by preincubating with a 2-fold molar excess of TCEP over GSH in 10 mM ammonium bicarbonate buffer, pH 7.4, for 4 h at 37 °C, followed by treatment with a 2-fold molar excess of NPM for 16 h at 37 °C.

Fluorescence Measurements. Steady-state fluorescence analyses were performed on a Perkin-Elmer LS55B fluorometer at 24 °C. Fluorescence emission spectra of pyrene-labeled samples were recorded in PBS between 350 and 550 nm by setting the excitation wavelength at 345 nm; those of AEDANS-labeled samples were collected between 350 and 600 nm followed by excitation at 345 nm. The excitation and emission slit widths

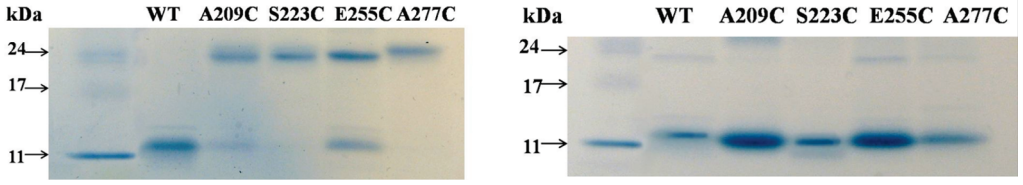

FIGURE 2: Intermolecular disulfide bond formation and dimerization in single Cys apoE CT variants. SDS−PAGE analysis (4−20% acrylamide gradient) of purified apoE CT WT, A209C, S223C, E255C, and A277C was carried out under nonreducing (left) and reducing (right) conditions. Disulfide bond formation was noted in all single Cys variants under nonreducing conditions but not in WT apoE CT.

were set at 5 nm. The scan speed was 50 nm/min; typically 10 scans were averaged. In experiments following the effect of disrupting tertiary structures, the samples were mixed with a 1:1 mixture of TFE and PBS. Fluorescence quenching analyses were carried out by addition of small increments of stock solutions of KI to 250 μL of 10 μg/mL pyrene-labeled apoE CT variants in PBS. The KI stock solutions contained 1 mM sodium thiosulfate to prevent formation of free iodine. The fluorescence emission intensities were recorded at 386 nm in the absence and the presence of varying amounts of KI. To account for possible salt effects on the structure due to the addition of large amounts of the quencher KI, parallel fluorescence measurements were performed in the presence of KCl; the chloride ion does not cause fluorescence quenching, since it is far smaller in size compared to the iodide ion. The presence of salt does not affect the fluorescence emission properties of pyrene-labeled apoE CT variants. Lastly, the order of unfolding of the helices was followed as changes in secondary and in tertiary/quaternary structures by CD and fluorescence spectroscopy, respectively. Accordingly, the percent maximal change in the ellipticity (θ) or fluorescence intensity (F) provided an indication of the overall changes in secondary and tertiary structure, respectively, and was calculated as follows:

$$((\theta \text{ (or } F) \text{ at 0 M GdnHCl} - \theta \text{ (or } F) \text{ at a given concentration of GdnHCl})/(\theta \text{ (or } F) \text{ at 0 M GdnHCl} - \theta \text{ (or } F) \text{ at 6 M GdnHCl})) \times 100$$

The ellipticity of WT apoE CT (0.2 mg/mL) or the fluorescence emission spectra of AEDANS-apoE CT variants (10 μg/mL) (excitation at 345 nm) were recorded following incubation of samples with varying concentrations of GdnHCl (0−6 M) in 50 mM sodium phosphate, pH 7.4, for 16 h at 24 °C. The fluorescence emission intensity at 482 nm was used for calculating percent maximal changes. The concentration of GdnHCl required to cause a 50% decrease in the maximal change, $[\text{GdnHCl}]_{1/2}$, was calculated for each construct.

RESULTS

The structural organization of the apoE CT and details regarding the mode of interaction between and within the monomers at the C-terminal end of apoE are not known. To address this issue, we employed site-directed fluorescence labeling with spatially sensitive fluorophores probing defined segments of the domain, as schematically represented in Figure 1B. The probes were located at positions 223 and 255 to monitor the two ends of the proposed class A helix and at position 277 to probe the class G* segment. In addition, as a control, we placed a probe at position 209, a location predicted to be outside the helical segment. The cysteine residues were substituted at these locations by site-directed mutagenesis (*28*). WT apoE CT lacks Cys residues and was included as a control when required. The probe of choice for evaluating spatial proximity was pyrene, which was attached to single cysteine residues using standard maleimide chemistry (*30*, *31*).

In our initial studies, we evaluated the possibility of intermolecular disulfide bond formation between the subunits of apoE CT in their naturally folded state in buffer. SDS−PAGE analysis was carried out under nonreducing and reducing conditions (Figure 2). Under nonreducing conditions, a 26 kDa band corresponding to the molecular mass of a disulfide-bonded dimer was observed in all cases except the WT protein (Figure 2, left). In the case of apoE CT E255C, there appears to be a mixture of disulfide-bonded and non-disulfide-bonded species. Nevertheless, the presence of the dimers is indicative of spatial proximity between cysteines at a given location on neighboring molecules. Under reducing conditions, the variants migrate with a mobility corresponding to that of monomeric apoE CT (Figure 2, right).

CD analysis was performed to verify the secondary structure of the variants in comparison with that of the WT protein. The analyses were carried out in their disulfide-bonded or reduced states. All variants adopt an α-helical structure similar to that of WT apoE CT in both states. Figure 3 shows representative spectra of the WT apoE CT and apoE CT S223C. The α-helical content was ~70% as calculated using the molar ellipticity at 222 nm; this is comparable to that of WT apoE CT, indicating that the substitution with a Cys residue does not alter the overall fold of the protein. Upon labeling with pyrene, the protein retains its overall global fold and structure with a small decrease (~10%) in the α-helical content (Figure 3B). This change is within the experimental variability and range noted between different preparations. Similarly, we confirmed that neither the substitution of single cysteine residues at other locations (such as 209, 255, and 277) nor labeling with a fluorophore significantly altered the overall fold of apoE CT (data not shown).

The extent of pyrene labeling was evaluated using the molar extinction coefficients for the protein (at 280 nm) and pyrene (at 345 nm) (16500 M^{-1} cm^{-1} and 40000 M^{-1} cm^{-1}, respectively). The calculations revealed that the labeling was never > 100%; in addition, WT apoE CT was not labeled. These observations indicate lack of nonspecific labeling of the different single cysteine variants.

In the next step, tertiary structural analysis was performed using the fluorescence emission characteristics of 5−10 μg/mL pyrene-apoE CT variants in PBS (Figure 4). Pyrene fluorescence emission spectra display two unique features that yield valuable information regarding spatial proximity and the polarity of the environment where the probe is located:

(*i*) *Monomer/Excimer Ratio Reflects Spatial Proximity*. When two pyrene rings are within 10 Å of each other, they form a dimer in the excited state (thus the term "excimer"). The excimer is seen as a broad unstructured band centered around 460 nm and

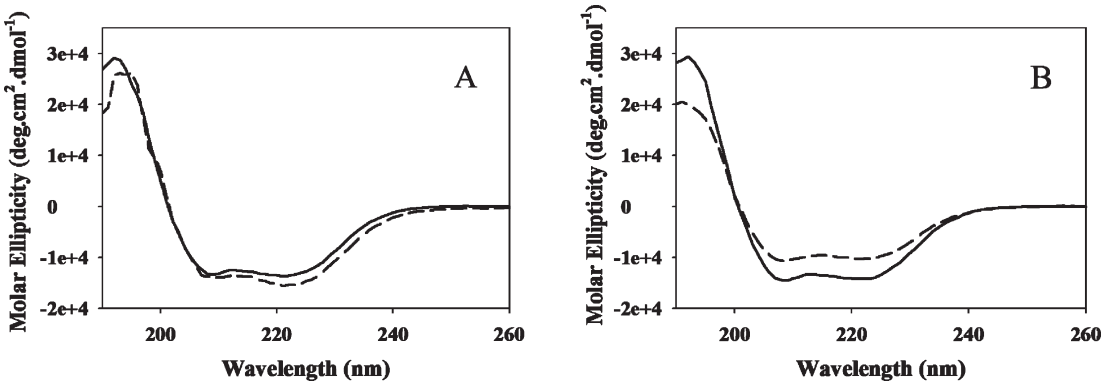

FIGURE 3: Far-UV CD spectra of WT and apoE CT S223C. Far-UV CD spectra of WT (0.2 mg/mL) in the presence (solid line) and the absence (dashed line) of 5-fold molar excess of TCEP (A). CD spectra of S223C apoE CT (0.2 mg/mL) in the absence of TCEP (solid line) and pyrene-labeled apoE CT S223C (dashed line) (B). Spectra were recorded from 185 to 260 nm in 10 mM ammonium bicarbonate buffer, pH 7.4. An average of three scans was collected, using a 0.1 cm path length cell, scan speed of 20 nm/min, and response time of 1 s.

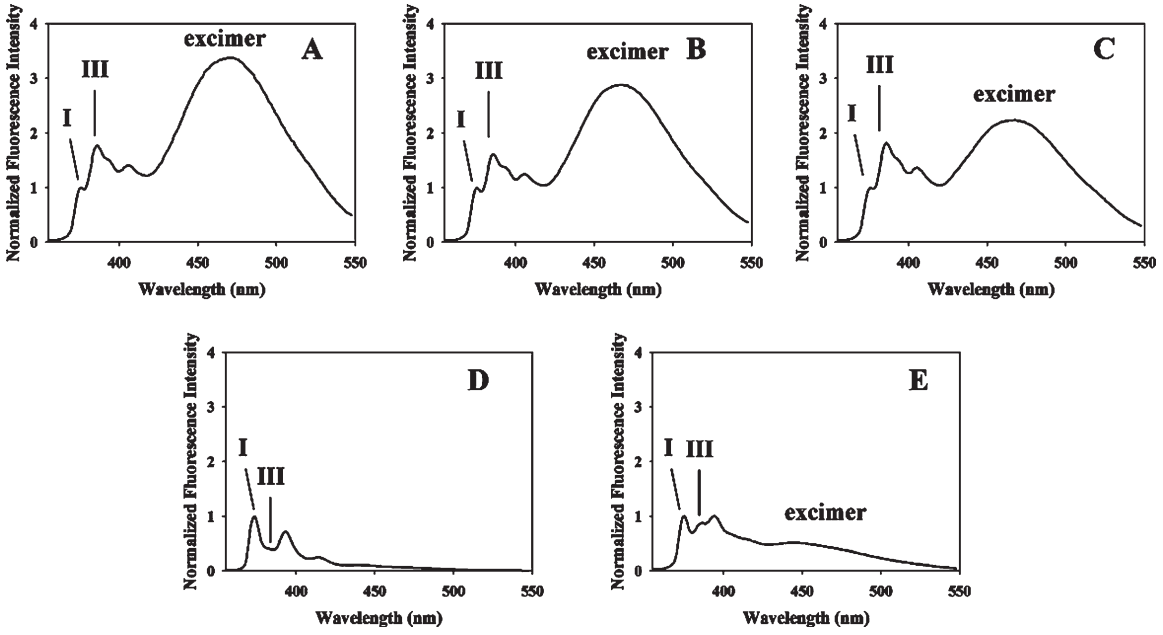

FIGURE 4: Fluorescence emission spectra of pyrene-labeled apoE CT variants report on spatial proximity and microenvironment polarity. Fluorescence emission spectra of apoE CT labeled with pyrene at positions 223 (A), 255 (B), and 277 (C). The protein concentration in each case was 5 μg/mL. The spectra shown are an average of 10 scans (recorded at a scan speed of 50 nm/min) with the excitation wavelength set at 345 nm (excitation and emission slit widths set at 5 nm). Arrows point to band I and band III at 375 and 386 nm, respectively. Emission spectra of 50 μg/mL GS-pyrene (D) and 5 μg/mL pyrene-labeled apoE CT A209C (E) were recorded as controls.

appears in addition to the monomeric family of bands that usually occurs between 375 and 405 nm (described below). The monomer/excimer (m/e) ratio, calculated by comparing the fluorescence intensity of the first monomer peak at 375 nm peak with respect to the excimer band at 460 nm, is a *relative* indicator of the extent of excimer formation and therefore the spatial proximity between two pyrene moieties (*31*−*35*). While the absolute values of the m/e ratio yield little information by themselves, comparison of ratios of a given set of labeled proteins provides details regarding the relative proximity between specified sites. In the case of apoE CT variants, we will be making inferences regarding intermolecular spatial proximity between apoE CT monomers or subunits since we have single Cys proteins, the polarity of their microenvironment, and/or orientation of a helical segment in one monomer with respect to the corresponding segment in a neighboring molecule. It is noteworthy that all three pyrene-apoE CT variants display an intense excimer band (Figure 4 A−C). The spectra have been normalized with respect to the peak at 375 nm. On average, the m/e ratios for pyrene-apoE CT S223C, E255C, and A277C are 0.30, 0.38, and 0.55, respectively. The presence of the intense excimer band and the low m/e ratios indicate that the pyrene moieties from neighboring subunits are located within 10 Å of each other.

It is possible that the hydrophobic rings of a polycyclic aromatic hydrocarbon such as pyrene may drive intermolecular interactions between monomeric apoE CT subunits, rather than protein−protein interactions of the hydrophobic faces of the amphipathic helices. This can be expected to lead to the formation of the excited state pyrene−pyrene dimers noted as the excimer emission band. To investigate this possibility, we evaluated the fluorescence emission characteristics of (i) a small peptide bearing a single pyrene, without the encumbering effect of a helix, and (ii) apoE CT bearing a single pyrene at a site that is not predicted to be in a helical segment. Toward this end, the fluorescence emission spectrum of pyrene-labeled glutathione (GS-pyrene), a polar tripeptide with a single Cys residue, was

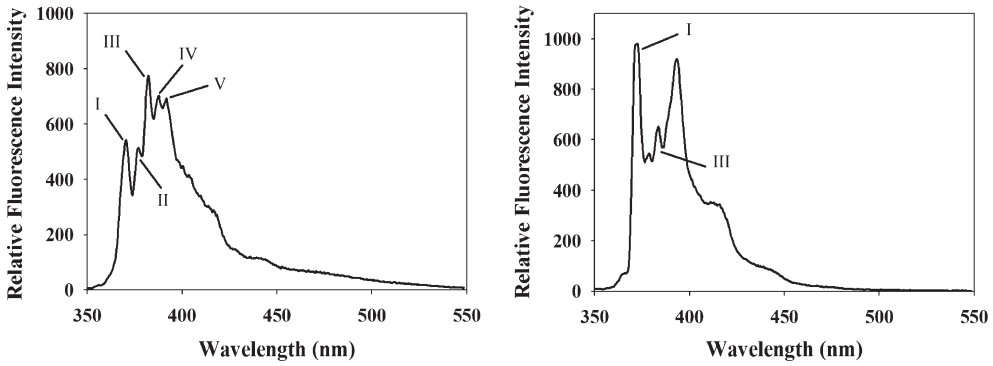

FIGURE 5: Pyrene fluorescence emission is sensitive to solvent polarity. The effect of solvent polarity on the fluorescence emission characteristics of pyrene was followed by recording the spectra of free pyrene in hexane (left) and DMSO (right). The dielectric constant and dipole moment of the solvents were used as indicators of their polarity, with hexane (low dielectric constant of ~4.8 and dipole moment of 0 D) considered a relatively nonpolar solvent and DMSO (high dielectric constant of ~47.2 and polarity of 3.96 D) considered a relatively polar solvent. Arrows point to bands I, II, III, IV, and V for hexane; only bands I and III are shown for DMSO.

recorded (Figure 4D). No excimer band was noted even at molar concentrations 1000-fold higher than that used for pyrene-apoE CT variants. The lack of excimer emission (*m*/*e* ratio of 13.6) confirms that the hydrophobic nature of the pyrene moiety and its associated tendency to undergo a stacking interaction are not significant contributory factors for the observation of the excimer emission band in the case of pyrene-apoE CT variants. Further, in an independent approach, we placed pyrene at position 209, which is predicted to lie outside the helical segment (*21*). The fluorescence emission spectrum of pyrene-apoE CT A209C (Figure 4E) displayed a significantly lower excimer emission band, with the *m*/*e* ratio being 1.82 ± 1.2. The higher *m*/*e* ratio is indicative of the probes at position 209 from two neighboring molecules being farther apart (≫10 Å) from each other. Lastly, it must be noted that the intensity of the excimer band was not the same for all of the different pyrene-labeled apoE CT variants studied, which would be the case if the hydrophobic nature of the pyrene rings is a significant factor in protein−protein interaction. Thus, while an enhancing effect of the presence of pyrene on driving the helix−helix interactions cannot be absolutely excluded, we believe that it is the intrinsic tendency of the amphipathic α-helices of apoE CT to make extensive helix−helix contact via their nonpolar face that makes the pyrene rings to be spatially proximal, a conclusion supported by the known self-association ability of apoE.

(*ii*) *Py Scale Reflects Polarity of the Microenvironment of Pyrene*. An empirical relationship has been established between pyrene fluorescence emission band ratios and solvent polarity (*36*−*38*). The $\pi \rightarrow \pi^*$ monomeric fluorescence emission spectrum of pyrene is described by an ensemble of five major vibronic bands designated bands I, II, III, IV, and V, corresponding to peaks at ~375, 379, 385, 395, and 405 nm, respectively. Since the electronic and vibronic states are coupled (*39*−*41*), the peak at 385 nm, labeled as the third vibronic band with 0−2 transition, is exquisitely sensitive to the polarity of the probe's microenvironment. It shows increased fluorescence emission intensity in comparison to the 375 nm peak or the first vibronic band (0−0 transition) intensity in hydrophobic environments. In contrast, the intensity of band I is significantly higher than that of band III in polar environments (*42*, *43*). This sensitivity and dependence on the polarity are illustrated in Figure 5, which shows the emission spectra of free pyrene in two different solvents, hexane (left) and dimethylsulfoxide (DMSO) (right). Hexane and DMSO represent solvents with low and high dielectric constants (4.8 and 47.2, respectively). The dipole moment for these solvents are 0 and 3.96 D, respectively. In hexane, pyrene displays a dominant peak at 385 relative to the 375 peak, while in DMSO the 375 peak is dominant, compared to the 385 peak. The reasons for these observations have been attributed to excited state interaction of the molecule with the surrounding solvent (H-bonding and other interactions between the solute dipole moment and that of the solvent) and solvent reorientation around the excited state dipole (*44*, *45*). Thus, by comparing the ratio of the relative intensities of band I to band III, which is referred to as the *Py scale*, it is possible to infer the polarity of the site in the vicinity of the probe (*34*, *37*, *40*, *46*, *47*). For pyrene-S223C, pyrene-E255C, and pyrene-A277C, the intensity of band III is ~2-fold higher than that of band I (*Py* scale of 0.56 ± 0.020, 0.62 ± 0.064, and 0.55 ± 0.018, respectively) (Figure 4A−C). This suggests a relatively hydrophobic microenvironment in the vicinity of positions 223, 255, and 277. In comparison, the *Py* scale for pyrene-A209C was 1.14, indicating a highly polar microenvironment, while that for GS-pyrene was even higher (1.23).

Fluorescence emission spectra of pyrene-labeled variants in the presence of 50% TFE are shown in Figure 6. TFE is a solvent that disrupts quaternary and tertiary structures but enhances secondary structural elements in proteins (*48*−*50*). In all cases, including pyrene-apoE CT A209C, the excimer emission decreased dramatically in the presence of TFE. In addition, the intensity of the 375 nm increased significantly with respect to band III intensity. This trend suggests exposure of pyrene to a relatively aqueous environment in the presence of TFE. The decrease suggests that the excited state dimer formation arises from quaternary interaction between two apoE molecules.

In an independent approach to assess the nature of the probe microenvironment, fluorescence emission of the pyrene probe was subjected to quenching by an aqueous quencher, KI, added in incremental amounts. Figure 7 (top) shows a plot of F/F_0 versus KI concentration, where F_0 and F are the fluorescence intensities at 386 nm in the absence and presence of varying amounts of KI, respectively. Pyrene fluorescence is quenched to varying extents by iodide depending on its location and qualitatively appears to follow the order 209 > 255 > 223 > 277. The quenching data can also be quantitatively represented as the Stern−Volmer plot, obtained by plotting F_0/F versus [KI] based on the equation shown below, where K_{SV} is the

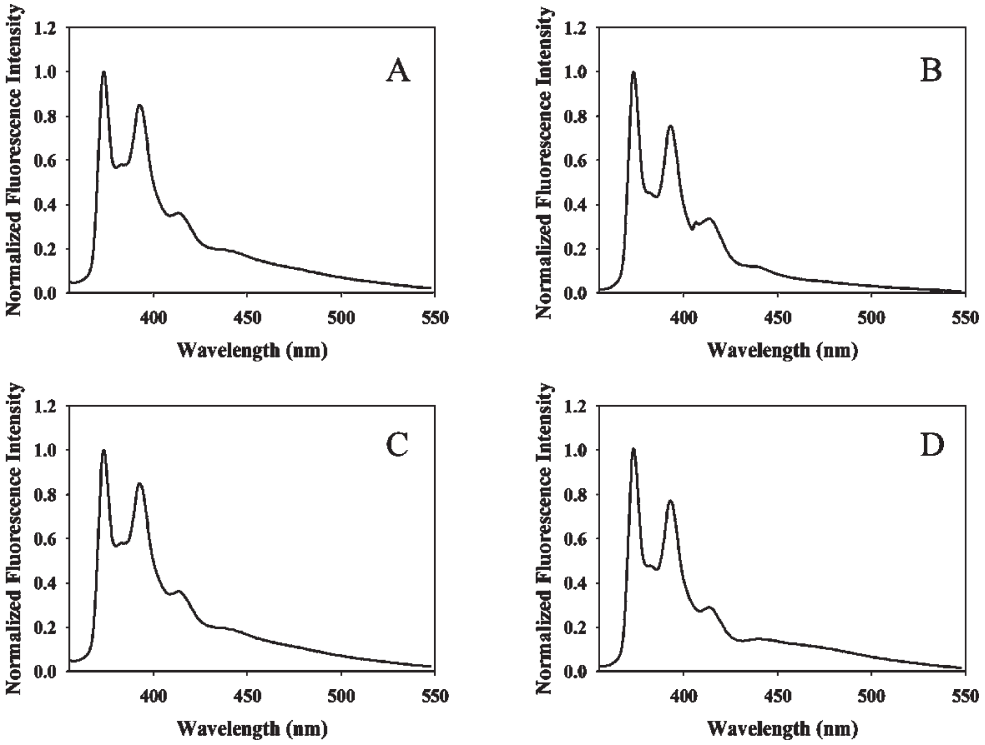

FIGURE 6: Fluorescence emission spectra of pyrene-labeled apoE CT variants with disrupted tertiary and quaternary interactions. Fluorescence emission spectra of pyrene-labeled apoE CT A209C (A), S223C (B), E255C (C), and A277C (D) were recorded in the presence of 50% TFE in PBS. Fluorescence measurements were carried out as described under Figure 4.

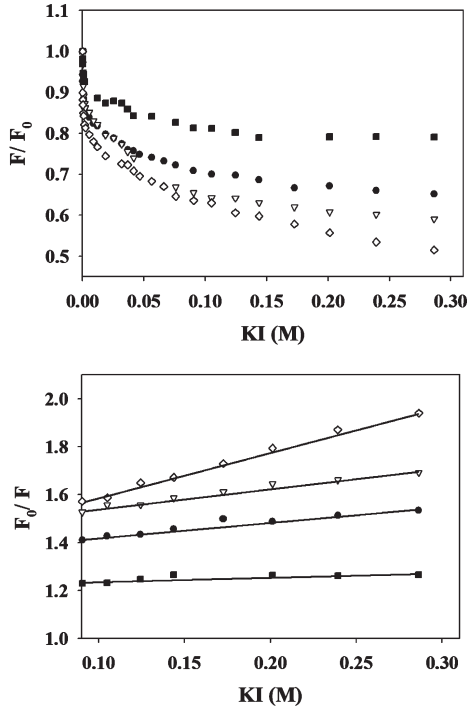

FIGURE 7: Quenching of pyrene fluorescence emission by KI. The fluorescence emission intensity of pyrene-labeled apoE CT A209C (open diamonds), S223C (filled circles), E255C (open triangles), and A277C (filled squares) was followed at 386 nm in the absence (F_0) or the presence (F) of increasing concentrations of KI. Plot of F/F_0 versus KI concentration (top). Since the K_{SV} plot of the entire range of [KI] shows a distinct curvature, the segment between 0.1 and 0.3 M KI was plotted versus F_0/F (bottom) to obtain apparent K_{SV} values. A representative plot from three different experiments is shown.

Stern−Volmer quenching constant and [Q] is the concentration of the quencher (*26*, *51*):

$$F_0/F = 1 + K_{SV}[Q]$$

The K_{SV} plot shows distinct curvature and departure from linearity in all cases and therefore could not be fitted into a straight line intersecting at 1 on the *Y*-axis. However, from a linear segment of the plot selected to reflect the trend observed in the F/F_0 versus [KI] plot, apparent K_{SV} values were calculated to be 1.93, 0.60, 0.74, and 0.17 for the probes at positions 209, 223, 255, and 277, respectively (Figure 7 (bottom)).

Lastly, GdnHCl-induced unfolding of apoE CT was evaluated by fluorescence analysis. Whereas CD measurements allow monitoring changes at the secondary structural level, fluorescence measurements allow us to monitor localized tertiary structural changes at selected sites on the protein. AEDANS was the probe of choice for this purpose since pyrene displayed anomalous spectral behavior in the presence of GdnHCl. A decrease in the emission intensity of AEDANS is interpreted as exposure of the probe to the aqueous environment due to localized unfolding. Changes in the fluorescence emission intensity of AEDANS at position 223, 255, or 277 were plotted as percent maximal change versus GdnHCl concentration (Figure 8). It is noteworthy that the denaturation profile for AEDANS at position 223 was distinctly different from that of either position 255 or 277 and was characterized by an initial resistance to unfolding at lower GdnHCl concentrations. The concentrations of GdnHCl required to elicit a 50% decrease in emission intensity ($[GdnHCl]_{1/2}$) for AEDANS at positions 223, 255, and 277 are 0.76, 0.73, and 0.59 M, respectively. The decrease in fluorescence intensity was accompanied by a change in the wavelength of maximal fluorescence emission from 480 to

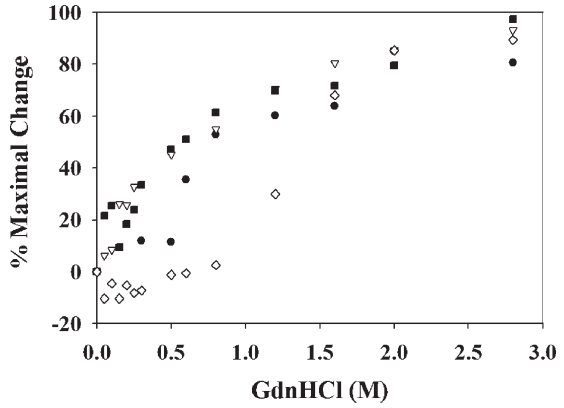

FIGURE 8: GdnHCl-induced unfolding of apoE CT. To follow GdnHCl-induced changes in the overall secondary and tertiary/quaternary structures, the percent maximal change in ellipticity (open diamonds) of WT apoE CT (0.2 mg/mL) or in fluorescence intensity of AEDANS-apoE CT variants (10 μg protein) was plotted as a function of GdnHCl concentration. AEDANS was located at position 223 (filled circles), 255 (open triangles), or 277 (filled squares).

499 nm as a function of increasing GdnHCl for all variants. AEDANS at position 209, being in an unstructured segment to start with, did not yield interpretable results (data not shown), especially at the low GdnHCl concentrations.

DISCUSSION

The tendency of apoE CT to self-associate makes it difficult to analyze this domain structurally by conventional high-resolution techniques. Thus, details regarding the tertiary and quaternary conformation of apoE CT domain are lacking. Since apoE3 bears a single Cys at position 112 in the NT domain, and since there is a possibility of interaction between the NT and CT domains in an apoE isoform-specific manner in the intact protein (*52*), for our studies we employed the independently folded isolated apoE CT but retained the residue numbering of the intact full-length protein. Pyrene was the probe of choice because of its ability to relay information not only on the spatial proximity of given segments but also on the polarity of the local microenvironment. An additional desirable feature is its property of emitting fluorescence only upon covalent attachment to thiols.

Our previous studies suggested that a large segment of the apoE CT may be involved in intermolecular coiled-coil helix formation leading to a dimer (*27*), with the possibility that two dimers further dimerize yielding a tetramer. They were based on secondary structural predictions and CD analysis that was carried out with protein concentrations as high as 0.2 mg/mL and therefore lacked the resolution needed to define the involvement of specific segments of the protein. In the present study, we circumvented these issues by employing pyrene fluorescence spectroscopy, which allows us to work with concentrations as low as 5−10 μg/mL labeled protein due to the high extinction coefficient of pyrene (40000 M^{-1} cm^{-1}).

Our results demonstrate that pyrene exhibits excimer emission regardless of its location on the different predicted helical segments of apoE CT. An interesting observation regarding these excimer bands is the extremely high intensity of their emission relative to the monomer peak at 375 nm. From our prior experience with structural analysis with apolipoproteins (*31*, *35*, *53*, *54*), such high-intensity excimer emission has not been noted before. The present observation indicates that the specified sites 223, 255, and 277 on one molecule are in intimate contact with corresponding sites on a neighboring apoE CT molecule. Unlike fluorescence resonance energy transfer analysis, measurement of pyrene excimer intensity has been routinely used for a qualitative assessment of distance between specified sites; to our knowledge there are no reports of a correlation between the absolute *m*/*e* ratio and the distance of separation. However, we made an interesting observation that the *m*/*e* ratio follows the order 277 > 255 ≥ 223, suggesting that the intermolecular distance around 223 is closer than that at position 277 from two molecules. More studies are needed to understand the correlation between the *m*/*e* ratio and distance of separation. Nevertheless, the high excimer intensity observed regardless of the location suggests that both the class A and class G* helices align with corresponding segments in the surrounding molecules of apoE CT, establishing extensive intermolecular helix−helix interactions in the lipid-free state. At this point we exclude intramolecular interactions since there is only one or less pyrene on a given subunit of apoE CT based on the labeling stoichiometry calculations. Further, the absence of an excimer band in GS-pyrene and pyrene-A209C apoE CT indicates that the stacking interactions of the hydrophobic aromatic pyrene rings are not the driving force for apoE self-association.

The band I/III ratio for the different variants provides further information regarding the probe microenvironment. The presence of a pronounced band III peak for pyrene located at positions 223, 255, and 277 (*Py* scale of ~0.4) indicates that these sections are in a hydrophobic environment as in a helix−helix interface. In concurrence, A209C, which is located immediately outside the helical segment, elicits a band I/III ratio of >1.0, reflecting a polar microenvironment. The disappearance of the broad excimer band at ~460 nm and the increase in intensity of band I in the presence of TFE indicate that the probes in all four sites relocate to a relatively polar environment with minimal helix−helix contact. These observations are consistent with the reported effects of this cosolvent on protein structure: stabilizing α-helical and β-turn elements and disruption of tertiary and quaternary structures. Strengthening local interactions and disfavoring nonlocal interactions, TFE appears to act by favoring internal H-bonds and altering hydrophobic interactions (*55*). The results with TFE confirm that the entire apoE CT has extensive quaternary interaction with neighboring molecules.

Further support for this concept is provided by fluorescence quenching by KI, an aqueous collisional quencher. Pyrene at position 277 was quenched to the least extent, while that located at position 209 was quenched maximally. This indicates that position 277 is in a buried location such as in the interior of a helix−helix interface. On the other hand, position 209 was significantly more accessible than other locations studied; this observation is consistent with the relatively lower intensity of band III and its predicted location in the relatively unstructured loop region. The observation that pyrenes at 223 and 255 are of intermediate accessibility to iodide quenching (less accessible compared to that at position 209 but more than that at 277) suggests that these sites are in a partially buried location and/or in a microenvironment containing negatively charged side chains that may repel the iodide ions. Additionally, quenching analysis also indicates that there are different populations of pyrene in solution, despite indications from stoichiometric calculations that there was one (or less than one) pyrene per apoE CT monomer. From the nonlinear Stern−Volmer plots, we suggest that the apoE CT adopts multiple conformations and/or

self-associated states or that the observed results are due to a combination of static and dynamic quenching (*56*).

Lastly, the GdnHCl-induced unfolding pattern of selected sites on apoE CT yielded valuable insights into the possible mode of intermolecular interaction. In previous studies, others and we noted that the $[GdnHCl]_{1/2}$ for loss of secondary structure was ~1.0 M based on CD analysis (*13*, *27*). At low GdnHCl concentrations (~0.3 M), the protein displayed secondary structural characteristics similar to that in the absence of denaturant. In the present study, we monitored changes in localized tertiary and quaternary conformation as a result of GdnHCl-induced protein unfolding. As expected, a lower $[GdnHCl]_{1/2}$ was noted in general by fluorescence analysis (regardless of probe location in the CT) when compared to the decrease noted by CD spectroscopy, suggesting that a loss in tertiary/quaternary conformation precedes the loss in the secondary structure. It is possible that the presence of AEDANS causes minor perturbations in the immediate microenvironment of the probe; however, bearing in mind that the extent of perturbation may be similar in the different locations (given that there was a similar extent of labeling), we noted distinct trends in the unfolding pattern depending on the location of the probe. The segment in the vicinity of positions 255 and 277 appears to be losing tertiary/quaternary organization at lower GdnHCl concentrations than that around position 223 (at 0.5 M GdnHCl, the segment around 255 and 277 is largely unfolded, while that around 223 is largely folded). This differential response to GdnHCl suggests possible differences in localized tertiary/quaternary structural organization, with the terminal helix of the apoE CT likely making a loosely packed helix−helix contact (such as an intermolecular helix bundle); on the other hand, the N-terminal end of this domain likely makes a tightly packed helix−helix contact (such as an intermolecular coiled-coil helix). Taken in conjunction with the possibility that the intermolecular distance around position 223 may be closer than that at position 277 (based on the *m*/*e* ratio for position 277 being higher than that for position 223), we propose a putative unfolding pattern as 277 unfolding first, followed or accompanied by 255, and then finally 223. This order of unfolding may be reflective of the order in which these helices may interact with a lipid surface. This observation suggests that the C-terminal end bearing the class G* helix likely unfolds prior to the class A helix toward the N-terminal end of the apoE CT.

In earlier studies (*25*), gel filtration analysis of truncated apoE missing residues 224−299, 245−299, or 267−299 indicated that the proteins eluted with apparent molecular weights close to that of dimers (ranging 40000−66000). The calculated molecular weights for these constructs were 25701, 28223, or 30883. While the authors considered dimers as possible candidates, their interpretation regarding the monomeric nature of these truncated variants was based on sedimentation equilibrium analysis (due to the anomalous behavior of proteins in gel filtration chromatography). Therefore, they attributed residues 268−289 in the terminal helix to apoE self-association in the absence of a lipid or lipoprotein surface to form dimers, tetramers, and possibly higher state oligomers (*14*). It is possible that the gel filtration results represent an equilibrium mixture of monomers and dimers. Additionally, the truncation may result in weak helix−helix interactions that may be dissociated under the centrifugal force applied in the sedimentation equilibrium analysis. On the basis of our spectroscopic analysis, we extend their proposal to state that the entire CT (210−299) is involved in

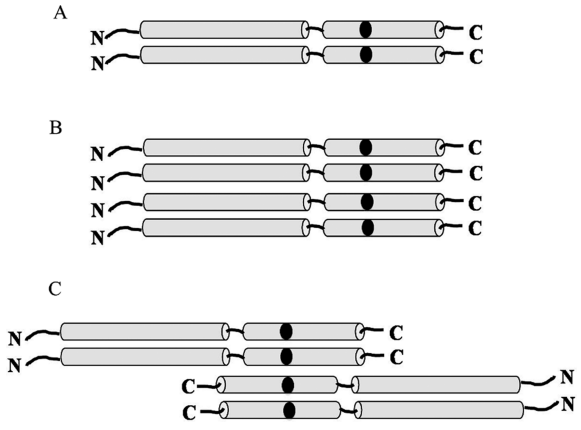

FIGURE 9: Proposed model for apoE CT self-association. Our results indicate that the entire apoE CT segment of one apoE molecule associates with a second apoE CT; the dimeric form of apoE CT further self-associates in either a parallel or antiparallel orientation. This is illustrated using position 277 (black oval). (A) Monomers self-associating to a parallel dimer. Dimers may dimerize further to form a parallel (B) or antiparallel (C) tetramer.

helix−helix contacts with neighboring molecules (i.e., both of the predicted amphipathic helices). Consistent with this suggestion, subsequent efforts to generate monomeric apoE for NMR analysis involved substituting residues at positions 257, 264, 269, 279, and 287, indicating that residues in the first and terminal predicted helices are likely involved in protein−protein contacts (*23*, *24*). Further, in a recent study examining the self-associated state of apoE3 missing residues 273−299 at 5 μg/mL concentration, Sakamoto and colleagues report a decrease in the tetramerization ability by gel filtration analysis using radiolabeled variants (*26*); this observation was based on altered monomer−tetramer distribution. Indeed, their gel filtration profile suggests the presence of dimers, an observation consistent with our current findings that the class A helix is involved in dimer formation as well.

In conclusion, we extend previous observations by others and us with our present results, which suggest that residues 210−299 (i.e., almost the entire CT of apoE) make extensive intersubunit helix−helix contacts to form a dimer (Figure 9A), which then dimerizes further to form a tetramer (Figure 9B,C). Direct evidence for this conclusion comes from the intense band III peak and excimer band noted for the three probes chosen to monitor different segments of the CT. Other studies have indicated that the enhanced peak intensity at 387 nm reflects exclusion of water (*43*); in the present case, it is interpreted that this enhanced intensity is due to close helix−helix hydrophobic contact, which excludes water. An additional inference derived from our study is that apoE CT dimerizes in a parallel orientation; an antiparallel orientation would place the pyrene labels on two neighboring molecules further apart than 10 Å, leading to an absence of the excimer band. We also propose that the dimers dimerize further to yield a tetramer, with the terminal helices likely forming an intermolecular four-helix bundle. Our present results cannot distinguish between a parallel and antiparallel orientation of the dimers (Figure 9B,C). It is possible that the intense excimer band is due to parallel orientation of two dimers, which would result in four pyrene rings juxtaposed with each other. Additionally, in our previous study, we demonstrated a shift in equilibrium to monomer−dimer−tetramer mixtures from a predominantly tetrameric population by sedimentation equilibrium analysis when apoE CT is exposed to low concentrations

of GdnHCl (~0.3 M) (*27*), suggesting an initial dissociation of tetramers to form dimers. Taken in conjunction with observations that the protein retained secondary structure but had altered tertiary/quaternary conformation in the last, but not the first, helical segment at ~0.3 M GdnHCl, it seems likely that the dimers orient in an antiparallel manner to form a tetramer. Additional support is derived from the truncation analysis (*25*, *26*), which indicated that deletion of the last helix led to loss of tetramerization; if the dimers were oriented parallel, then the truncation would not have resulted in loss of tetramerization as they would still associate via residues 210−266. Thus, an antiparallel orientation of the dimers seems to be a plausible arrangement for the tetramer. More studies are needed to arrive at a more definitive tetramer model.

Lastly, it is important to note that the current studies were performed at ~5 μg/mL, which is a physiologically relevant concentration for apoE: the plasma level of apoE is in the range of 50 μg/mL (*57*), while the level in the central nervous system is predicted to be ~5 μg/mL (*58*). While a substantial fraction of this apoE may be in a lipid-associated state, it is believed that a significant amount of secreted apoE might be associated with cell surface proteoglycans in a lipid-free state. Lipid-free apoE is susceptible to protease cleavage, with the loop region linking the two domains being a "hot spot" for cleavage, yielding the apoE N-terminal domain and CT fragments. These apoE fragments are particularly prevalent in the aging brain and in age-related diseases such as Alzheimer's disease (*59*−*62*). apoE4 is also associated with neurotoxicity due to generation of the toxic N-terminal and CT fragments. The CT fragment can also potentially interact with the amyloid β peptide to form amyloid aggregates (*28*, *63*) and plaques in the brain of Alzheimer's disease patients. Thus, understanding the conformation of the apoE CT will yield valuable insights into the role of this domain in lipid metabolism and in disease states. Although they bear the same sequence in their C-terminal domains, apoE3 and apoE4 behave significantly different in several biochemical, biophysical, and physiological respects. Future studies will be aimed at determining the conformation of this domain in the context of the full-length protein and identifying specific differences in the conformation with respect to this domain between the isoforms.

ACKNOWLEDGMENT

We thank Dr. Vincent Raussens, Université Libre de Bruxelles, Brussels, Belgium, for help with the circular dichroism experiment and Darin Khumsupan for assistance in manuscript preparation.

REFERENCES

1. Mahley, R. W. (1988) Apolipoprotein E: cholesterol transport protein with expanding role in cell biology. *Science 240*, 622–630.
2. Zhang, S. H., Reddick, R. L., Piedrahita, J. A., and Maeda, N. (1992) Spontaneous hypercholesterolemia and arterial lesions in mice lacking apolipoprotein E. *Science 258*, 468–471.
3. Corder, E. H., Saunders, A. M., Strittmatter, W. J., Schmechel, D. E., Gaskell, P. C., Small, G. W., Roses, A. D., Haines, J. L., and Pericak-Vance, M. A. (1993) Gene dose of apolipoprotein E type 4 allele and the risk of Alzheimer's disease in late onset families. *Science 261*, 921–923.
4. Shimano, H., Ohsuga, J., Shimada, M., Namba, Y., Gotoda, T., Harada, K., Katsuki, M., Yazaki, Y., and Yamada, N. (1995) Inhibition of diet-induced atheroma formation in transgenic mice expressing apolipoprotein E in the arterial wall. *J. Clin. Invest. 95*, 469–476.
5. Mahley, R. W., Weisgraber, K. H., and Huang, Y. (2009) Apolipoprotein E: structure determines function, from atherosclerosis to Alzheimer's disease to AIDS. *J. Lipid. Res. 50* (Suppl.), S183–S188.
6. Fagan, A. M., Holtzman, D. M., Munson, G., Mathur, T., Schneider, D., Chang, L. K., Getz, G. S., Reardon, C. A., Lukens, J., Shah, J. A., and LaDu, M. J. (1999) Unique lipoproteins secreted by primary astrocytes from wild type, apoE (−/−), and human apoE transgenic mice. *J. Biol. Chem. 274*, 30001–30007.
7. Fagan, A. M., and Holtzman, D. M. (2000) Astrocyte lipoproteins, effects of apoE on neuronal function, and role of apoE in amyloid-beta deposition in vivo. *Microsc. Res. Tech. 50*, 297–304.
8. Von Eckardstein, A., Nofer, J. R., and Assmann, G. (2001) High density lipoproteins and arteriosclerosis. Role of cholesterol efflux and reverse cholesterol transport. *Arterioscler., Thromb., Vasc. Biol. 21*, 13–27.
9. Mahley, R. W., Huang, Y., and Weisgraber, K. H. (2006) Putting cholesterol in its place: apoE and reverse cholesterol transport. *J. Clin. Invest. 116*, 1226–1229.
10. Yokoyama, S. (2006) ABCA1 and biogenesis of HDL. *J. Atheroscler. Thromb. 13*, 1–15.
11. Mahley, R. W., Huang, Y., and Weisgraber, K. H. (2007) Detrimental effects of apolipoprotein E4: potential therapeutic targets in Alzheimer's disease. *Curr. Alzheimer Res. 4*, 537–540.
12. Yokoyama, S., Kawai, Y., Tajima, S., and Yamamoto, A. (1985) Behavior of human apolipoprotein E in aqueous solutions and at interfaces. *J. Biol. Chem. 260*, 16375–16382.
13. Wetterau, J. R., Aggerbeck, L. P., Rall, S. C., Jr., and Weisgraber, K. H. (1988) Human apolipoprotein E3 in aqueous solution. I. Evidence for two structural domains. *J. Biol. Chem. 263*, 6240–6248.
14. Aggerbeck, L. P., Wetterau, J. R., Weisgraber, K. H., Wu, C. S., and Lindgren, F. T. (1988) Human apolipoprotein E3 in aqueous solution. II. Properties of the amino- and carboxyl-terminal domains. *J. Biol. Chem. 263*, 6249–6258.
15. Perugini, M. A., Schuck, P., and Howlett, G. J. (2000) Self-association of human apolipoprotein E3 and E4 in the presence and absence of phospholipid. *J. Biol. Chem. 275*, 36758–36765.
16. Wilson, C., Wardell, M. R., Weisgraber, K. H., Mahley, R. W., and Agard, D. A. (1991) Three-dimensional structure of the LDL receptor-binding domain of human apolipoprotein E. *Science 252*, 1817–1822.
17. Wilson, C., Mau, T., Weisgraber, K. H., Wardell, M. R., Mahley, R. W., and Agard, D. A. (1994) Salt bridge relay triggers defective LDL receptor binding by a mutant apolipoprotein. *Structure 2*, 713–718.
18. Dong, L. M., Wilson, C., Wardell, M. R., Simmons, T., Mahley, R. W., Weisgraber, K. H., and Agard, D. A. (1994) Human apolipoprotein E. Role of arginine 61 in mediating the lipoprotein preferences of the E3 and E4 isoforms. *J. Biol. Chem. 269*, 22358–22365.
19. Forstner, M., Peters-Libeu, C., Contreras-Forrest, E., Newhouse, Y., Knapp, M., Rupp, B., and Weisgraber, K. H. (1999) Carboxyl-terminal domain of human apolipoprotein E: expression, purification, and crystallization. *Protein Expression Purif. 17*, 267–272.
20. Segrest, J. P., De Loof, H., Dohlman, J. G., Brouillette, C. G., and Anantharamaiah, G. M. (1990) Amphipathic helix motif: classes and properties. *Proteins 8*, 103–117.
21. Segrest, J. P., Jones, M. K., De Loof, H., Brouillette, C. G., Venkatachalapathi, Y. V., and Anantharamaiah, G. M. (1992) The amphipathic helix in the exchangeable apolipoproteins: a review of secondary structure and function. *J. Lipid Res. 33*, 141–166.
22. Segrest, J. P., Garber, D. W., Brouillette, C. G., Harvey, S. C., and Anantharamaiah, G. M. (1994) The amphipathic alpha helix: a multifunctional structural motif in plasma apolipoproteins. *Adv. Protein Chem. 45*, 303–369.
23. Fan, D., Li, Q., Korando, L., Jerome, W. G., and Wang, J. (2004) A monomeric human apolipoprotein E carboxyl-terminal domain. *Biochemistry 43*, 5055–5064.
24. Zhang, Y., Vasudevan, S., Sojitrawala, R., Zhao, W., Cui, C., Xu, C., Fan, D., Newhouse, Y., Balestra, R., Jerome, W. G., Weisgraber, K., Li, Q., and Wang, J. (2007) A monomeric, biologically active, full-length human apolipoprotein E. *Biochemistry 46*, 10722–10732.
25. Westerlund, J. A., and Weisgraber, K. H. (1993) Discrete carboxyl-terminal segments of apolipoprotein E mediate lipoprotein association and protein oligomerization. *J. Biol. Chem. 268*, 15745–15750.
26. Sakamoto, T., Tanaka, M., Vedhachalam, C., Nickel, M., Nguyen, D., Dhanasekaran, P., Phillips, M. C., Lund-Katz, S., and Saito, H. (2008) Contributions of the carboxyl-terminal helical segment to the self-association and lipoprotein preferences of human apolipoprotein E3 and E4 isoforms. *Biochemistry 47*, 2968–2977.
27. Choy, N., Raussens, V., and Narayanaswami, V. (2003) Inter-molecular coiled-coil formation in human apolipoprotein E C-terminal domain. *J. Mol. Biol. 334*, 527–539.

28. Tamamizu-Kato, S., Cohen, J. K., Drake, C. B., Kosaraju, M. G., Drury, J., and Narayanaswami, V. (2008) Interaction with amyloid beta peptide compromises the lipid binding function of apolipoprotein E. *Biochemistry 47*, 5225–5234.
29. Morrow, J. A., Segall, M. L., Lund-Katz, S., Phillips, M. C., Knapp, M., Rupp, B., and Weisgraber, K. H. (2000) Differences in stability among the human apolipoprotein E isoforms determined by the amino-terminal domain. *Biochemistry 39*, 11657–11666.
30. Haugland, R. P. (2005) The handbook, a guide to fluorescent probes and labeling technologies, 10th ed., Invitrogen Corp., Carlsbad, CA.
31. Sahoo, D., Narayanaswami, V., Kay, C. M., and Ryan, R. O. (2000) Pyrene excimer fluorescence: a spatially sensitive probe to monitor lipid-induced helical rearrangement of apolipophorin III. *Biochemistry 39*, 6594–6601.
32. Martinho, J. M. G. (1989) Heavy-atom quenching of monomer and excimer pyrene fluorescence. *J. Phys. Chem. 93*, 6687–6692.
33. Ahmed, O., and Yamamoto, S. (1995) Effects of the ring size and solvent polarity on the stability of the cyclic intramolecular excimer of saturated diamines. *J. Phys. Chem. 8*, 484–489.
34. Tedeschi, C., Mohwald, H., and Kirstein, S. (2001) Polarity of layer-by-layer deposited polyelectrolyte films as determined by pyrene fluorescence. *J. Am. Chem. Soc. 123*, 954–960.
35. Sahoo, D., Weers, P. M., Ryan, R. O., and Narayanaswami, V. (2002) Lipid-triggered conformational switch of apolipophorin III helix bundle to an extended helix organization. *J. Mol. Biol. 321*, 201–214.
36. Dong, D. C., and Winnik, M. A. (1982) The Py scale of solvent polarities. Solvent effects on the vibronic fine structure of pyrene fluorescence and empirical correlations with E_T and Y values. *Photochem. Photobiol. 35*, 1721.
37. Dong, D. C., and Winnik, M. A. (1984) The Py scale of solvent polarities. *Can. J. Chem. 62*, 2560–2565.
38. Acree, W. E. J., Tucker, S. A., Zvaigzne, A. I., Steet, K. W. J., Fetzer, J. C., and Grutzmacher, H. F. (1990) Polycyclic aromatic hydrocarbon solute probes. 7. Evaluation of additional coronene derivatives as possible solvent polarity probe molecules. *Appl. Spectrosc. 44*, 477.
39. Hara, K., and Ware, W. R. (1980) Influence of solvent perturbation on the radiative transition probability from the $^1B_{1u}$ state of pyrene. *Chem. Phys. 51*, 61.
40. Karpovich, D. S., and Blanchard, G. J. (1995) Relating the polarity-dependent fluorescence response of pyrene to vibronic coupling. Achieving a fundamental understanding of the py polarity scale. *J. Phys. Chem. 99*, 3951–3958.
41. Geigle, K. P., Wolf, J., and Hohlneicher, G. (1997) Franck-Condon/Herzberg-Teller interferences in the ^1L_b transitions of pyrene and chrysene. *J. Photochem. Photobiol. A: Chem. 105*, 183–187.
42. Nakajima, A. (1971) Solvent effect on the vibrational structures of the fluorescence and absorption spectra of pyrene. *Bull. Chem. Soc. Jpn. 44*, 3272–3277.
43. Kalyanasundaram, K., and Thomas, J. K. (1977) Environmental effects on vibronic band intensities in pyrene monomer fluorescence and their application in studies of micellar systems. *J. Am. Chem. Soc. 99*, 2039–2044.
44. Lakowicz, J. R. (1999) Solvent effects on emission spectra, in Principles of fluorescence spectroscopy, 2nd ed., pp 185−189, Kluwer Academic/Plenum, New York.
45. Nakajima, A. (1976) Effects of isomeric solvents on vibronic band intensities in fluorescence spectrum of pyrene. *J. Mol. Spectrosc. 61*, 467–469.
46. Winnick, F. M. (1993) Photophysics of preassociated pyrenes in aqueous polymer solutions and in other organized media. *Chem. Rev. 93*, 587–614.
47. Tamamizu-Kato, S., Kosaraju, M. G., Kato, H., Raussens, V., Ruysschaert, J. M., and Narayanaswami, V. (2006) Calcium-triggered membrane interaction of the alpha-synuclein acidic tail. *Biochemistry 45*, 10947–10956.
48. Lau, S. Y., Taneja, A. K., and Hodges, R. S. (1984) Synthesis of a model protein of defined secondary and quaternary structure. Effect of chain length on the stabilization and formation of two-stranded alpha-helical coiled-coils. *J. Biol. Chem. 259*, 13253–13261.
49. Frère, V., Sourgen, F., Monnot, M., Troalen, F., and Fermandjian, S. (1995) A peptide fragment of human DNA topoisomerase II alpha forms a stable coiled-coil structure in solution. *J. Biol. Chem. 270*, 17502–17507.
50. Gast, K., Zirwer, D., Muller-Frohne, M., and Damaschun, G. (1999) Trifluoroethanol-induced conformational transitions of proteins: insights gained from the differences between alpha-lactalbumin and ribonuclease A. *Protein Sci. 8*, 625–634.
51. Eftink, M. R., and Ghiron, C. A. (1976) Exposure of tryptophanyl residues in proteins. Quantitative determination by fluorescence quenching studies. *Biochemistry 15*, 672–680.
52. Dong, L. M., Parkin, S., Trakhanov, S. D., Rupp, B., Simmons, T., Arnold, K. S., Newhouse, Y. M., Innerarity, T. L., and Weisgraber, K. H. (1996) Novel mechanism for defective receptor binding of apolipoprotein E2 in type III hyperlipoproteinemia. *Nat. Struct. Biol. 3*, 718–722.
53. Sahoo, D., Narayanaswami, V., Kay, C. M., and Ryan, R. O. (1998) Fluorescence studies of exchangeable apolipoprotein-lipid interactions. Superficial association of apolipophorin III with lipoprotein surfaces. *J. Biol. Chem. 273*, 1403–1408.
54. Drury, J., and Narayanaswami, V. (2005) Examination of lipid-bound conformation of apolipoprotein E4 by pyrene excimer fluorescence. *J. Biol. Chem. 280*, 14605–14610.
55. Thomas, P. D., and Dill, K. A. (1993) Local and nonlocal interactions in globular proteins and mechanisms of alcohol denaturation. *Protein Sci. 2*, 2050–2065.
56. Lakowicz, J. R. (1999) Quenching of fluorescence, in Principles of fluorescence spectroscopy, 2nd ed., pp 237−249, Kluwer Academic/Plenum, New York.
57. Gregg, R. E., Zech, L. A., Schaefer, E. J., Stark, D., Wilson, D., and Brewer, H. B., Jr. (1986) Abnormal in vivo metabolism of apolipoprotein E4 in humans. *J. Clin. Invest. 78*, 815–821.
58. Linton, M. F., Gish, R., Hubl, S. T., Butler, E., Esquivel, C., Bry, W. I., Boyles, J. K., Wardell, M. R., and Young, S. G. (1991) Phenotypes of apolipoprotein B and apolipoprotein E after liver transplantation. *J. Clin. Invest. 88*, 270–281.
59. Marques, M. A., Tolar, M., Harmony, J. A., and Crutcher, K. A. (1996) A thrombin cleavage fragment of apolipoprotein E exhibits isoform-specific neurotoxicity. *Neuroreport 7*, 2529–2532.
60. Golabek, A. A., Soto, C., Vogel, T., and Wisniewski, T. (1996) The interaction between apolipoprotein E and Alzheimer's amyloid beta-peptide is dependent on beta-peptide conformation. *J. Biol. Chem. 271*, 10602–10606.
61. Tolar, M., Marques, M. A., Harmony, J. A., and Crutcher, K. A. (1997) Neurotoxicity of the 22 kDa thrombin-cleavage fragment of apolipoprotein E and related synthetic peptides is receptor-mediated. *J. Neurosci. 17*, 5678–5686.
62. Huang, Y., Liu, X. Q., Wyss-Coray, T., Brecht, W. J., Sanan, D. A., and Mahley, R. W. (2001) Apolipoprotein E fragments present in Alzheimer's disease brains induce neurofibrillary tangle-like intracellular inclusions in neurons. *Proc. Natl. Acad. Sci. U.S.A. 98*, 8838–8843.
63. Phu, M. J., Hawbecker, S. K., and Narayanaswami, V. (2005) Fluorescence resonance energy transfer analysis of apolipoprotein E C-terminal domain and amyloid beta peptide (1−42) interaction. *J. Neurosci. Res. 80*, 877–886.